



Anatomical structure segmentation from early fetal ultrasound sequences using global pollination CAT swarm optimizer-based Chan–Vese model

M. A. Femina¹ · S. P. Raajagopalan²

Received: 25 July 2018 / Accepted: 4 May 2019 / Published online: 12 June 2019

© International Federation for Medical and Biological Engineering 2019

Abstract

The structure of an early fetal heart provides essential information for the diagnosis of fetus defects. Accurate segmentation of anatomical structure is a major challenging task because of the small size, low signal-to-noise ratio, and rapid movement of the ultrasound images. In recent years, active contour methods have found applications to ultrasound image segmentation. The familiar region-based Chan–Vese (RCV) model is a strong and flexible technique that is able to segment many types of images compared to other active contours. However, the solution trapping in local minima is the main drawback determined on the RCV model with the exposure of improper initial contours. Also, the RCV model showed poor results with this situation. More probably, the images having large intensity differences between global and local structures usually suffered from this problem. To solve this issue, we develop an improved version of the RCV model which is expected to achieve satisfactory segmentation performance, irrespective of the initial selection of the contour. We have formulated a new and hybrid meta-heuristic optimization algorithm namely global pollination–based CAT swarm (GPCATS) optimizer to solve the fitting energy minimization problem. In the GPCATS method, the global pollination step of the flower pollination algorithm (FPA) is used for improving the distance averaging of the CATS algorithm. The performance of the proposed method was analyzed on different fetal heart ultrasound videos acquired from 12 subjects. Each frame of each video was manually annotated in order to provide labels for training and validating the model. Experimental results of the proposed model proved that the precision of locating boundaries is improved greatly and requires only a reduced number of iterations (75% less) for convergence compared to the traditional RCV model. This proposed method also proved that our model not only enhances the accuracy of locating boundaries but also works stronger robustness than some other active contour methods.

Keywords Congenital heart defect · Fetal heart · Ultrasound · Global pollination · CAT swarm · Chan–Vese · Level set

1 Introduction

Congenital heart defect (CHD) is a progressive heart disease commonly affecting the newborns (i.e., about 8 in every 1000 live births) [1, 2]. Prenatal

echocardiography is used to diagnose the CHD, where the rate of newborns death is in peak due to cardiac defect [3]. However, CHD can be predicted accurately using the fetal echocardiography. Also, this advanced echocardiography can diagnose the CHD in fetal life itself [4]. The merits of using fetal echocardiographs are as follows: (a) it allows safe transmission of ultrasound energy to a developing fetus, and (b) using the vaginal approach, the cardiac structures from 10 to 12 weeks of pregnancy itself can be studied; also, the transabdominal approach is used to study the cardiac structures from 16 to 18 weeks of pregnancy. For the fetal examination, the four-chamber view plays a significant role especially; it supports an examiner who is

✉ M. A. Femina
feminaphd@gmail.com; femijeni@yahoo.co.in

¹ Electrical and Electronics Engineering, KCG College of Technology, Chennai, India

² Computer Science and Engineering, GKM College of Engineering and Technology, Chennai, Tamil Nadu, India

not an expert in fetal echocardiography [5]. The extracardiac and/or other cardiovascular malformations can associate the congenital heart malformations, and for the detection of congenital heart defect, it is important to conduct an extended ultrasonic valuation of the fetus. The ultrasonic cine loop sequences of apical four-chamber view are comprised in the fetal echocardiogram and they are in a 2D model lasting only for a few seconds [6]. Furthermore, automatic detection of four chambers turns to be a challenging task in fetal echocardiography due to the presence of artifacts and missing contours, speckle noise, and gross intensity inhomogeneity. As an example, Fig. 1 is one typical four-chamber view in the fetal echocardiogram with gestational age = 21st week. It is observed that the fetal heart can be roughly classified into two groups: four cardiac chambers (including RA, LA, RV, and LV) and other regions outside the chambers. Normally, higher and inhomogeneous intensities are found in regions such as mitral tricuspid valve annuli and myocardium. Conversely, low intensities are found in the four cardiac chambers. Hence, convincing chamber segmentation is seen in this application.

Work in [7] presents that more time and high-skilled operation are required for diagnosing the fetal heart defects. Osher and Sethian [8] have introduced the level set methods, and these methods are adopted by many of the applications for tracking the evolution of fronts, segmenting the echographic images [9–15]. In medical image segmentation, the active contour approaches have proved its great strength. The existing active contour model can be distinguished into two types, region-based method [16–18] and edge-based method [18, 19]. Geodesic active contour (GAC) method was developed by N. Paragios et al. [20], which is the most popular edge-based segmentation technique based on the curve

evolution theory using image gradient. Nevertheless, it is usually sensitive to noise and weak edges. Conversely, Chan and Vese [16] developed the CV method based on Mumford–Shah model that is most generally used region-based active contour model for segmentation purpose. However, this method is computationally expensive, but it has much convergence range by incorporating the region-based information into the energy function.

According to Piccoli et al. [21], the 2D fetal echocardiographic images were segmented using neural networks. Detection of fetal heart abnormalities was supported by various computerized methods proposed in the past years. Lassige et al. [22] detected the spatial defects in 2D and 3D echocardiographic images using the level set algorithm. Siquiera et al. [23] have obtained the heart structure through segmenting the fetal heart using a k-means clustering and self-organizing map algorithm. Nonetheless, before segmenting the four-chambers of the fetal heart, the level set algorithm is improved using the shape in the work of Dindoyal et al. [24]. In many of the ultrasound applications like segmentation of echocardiograms, the deformable models have attained promising results [20, 25, 26]. However, these methods can be successful for some extent in the segmentation fetal cardiac defects as they are commonly known as semi-automated methods [27–30]. The presence of low signal-to-noise (SNR) ratio and small size of fetal hearts have degraded the clarity in ultrasound images of early fetal hearts [31].

Lin et al. [32] improved the idea of level set segmentation through providing interesting variant which integrates the region and edge information across the spatial scales in a level set approach. The statistical based shape information is incorporated into Caselles' geometric active contours model using the technique proposed by Leventon et al. [33]. But, the first few Eigen modes are given importance to perform this optimization. Later, to the same segmentation model, the different shape difference terms are combined with the work of Chen et al. [12]. A shape prior segmentation model was proposed by Cremers et al. [34], which takes into account the Mumford–Shah's functional to apply a statistically based shape before it, and also, a Chan–Vese's segmentation model is considered to incorporate a level set-based shape difference term into them using their newly developed variational approach [34]. Additionally, Hatice Çataloluk and Fatih Vehbi Çelebi [35] adopted the traditional gravitational search algorithm (GSA) and Chan–Vese method to develop a hybrid model that suits best for image segmentation. But initial contour selection is the only goodness observed in this hybrid model compared to the limitations of the traditional Chan–Vese and GSA approach. Also,

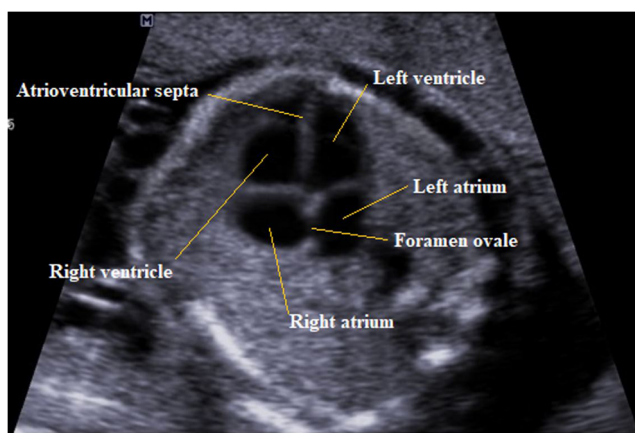


Fig. 1 Ultrasound image description: fetal heart with four-chamber view (gestational age = 21st week)

this method consumes more running time with large image size and feels hard for accurate adjustment of parameters to perform contour selection.

Automated segmentation is the major challenging task found on echocardiographic image sequences. The state-of-the-art works have proposed many methods for segmentation of echocardiographic data, and they are categorized into different classes as follows: database-guided (DB guided) segmentation, bottom-up approaches, active appearance models (AAM), active contour methods, active shape models (ASM), deformable templates, and level set (LS) approaches [36, 37]. Yan [38] adopted the fast marching method to apply the level set method on echocardiographic images. The speed term in this method is evaluated using an average intensity gradient-based measure, and this is done for minimizing the error occurrences on using the intensity gradient (local feature) measurements. The genetic algorithm is used by the active contour solution proposed by Mishra et al. [39] for its optimization. Hunter et al. [40] adopted the neural networks to develop an automatic segmentation method which aids in the detection of the left ventricle of the heart. A temporal learning filter is proposed by Malassiotis et al. [41], and they used an active contour model with this proposed filter to refine the epicardium segmentation. To the level set functions of training shapes sets, the PCA analysis is applied as stated in the work [16]. Boukerroui et al. [42] used a Bayesian network to perform robust adaptive region segmentation. Cremers et al. [43] proposed a non-linear statistical shape model, whereas based on an active shape model of Rousson et al. [44], the prior implicit shapes were analyzed. The application of active contour model was studied by Skalski et al. [45], and they observed that left ventricle segmentation in ultrasound echocardiographic images can be done without using the edge method. Currently, a geometric shape was introduced by Foulonneau et al. [46] where this shape was obtained prior to computing the distance among the currently segmented shapes and the Legendre moments of a set of representative shapes. In [47], the feature space was reduced using a PCA and, from this reduced space, the Legendre moments of a training shapes set obtained are used to develop a statistical shape model. In [48], from Legendre moments, the shape prior is formed and employed for cardiac segmentation on CT images by means of integrating them into a fuzzy region competition framework.

Notably, unique shape prior supports less when detected great variations on morphologies and positions of the fetus. According to the recent past works, the

clinical examinations are highly enhanced with the use of computer-aided diagnosis. Most of the cardiac anomalies can be diagnosed accurately using 2D US images [49]. The prenatal ventricular septal defect is identified while on performing the Markov random field segmentation. Furthermore, the medical experts can diagnose the heart defect earlier with the support of an effective ANFIS-based truncus arteriosus congenital heart defect (TACHD) detection technique [50].

None of the aforementioned literal works have provided details about the structure and differentiation of chambers from the adjacent tissue. However, the two main elements used for the diagnoses of fetal heart defect are chamber size and segmentation. A congenital cardiac abnormality can be detected by the way of chamber segmentation. Conversely, the congenital cardiac abnormalities such as hypoplastic left heart syndrome, the presence of echogenic intracardiac foci (EIF), persistent truncus arteriosus, endocardial cushion defects, large ventricular septal defects, AV canal defects, and septal defects can be detected with the fetal heart chamber position. Essentially, similar sized arterial chambers having foramen ovale flap opening at the left atrium are evaluated with the support of chamber segmentation. Furthermore, the morphology of the right ventricle placed behind the serum can be analyzed well using the ventricular chamber segmentation. Also, the defects such as interatrial and interventricular septa are identified using chamber segmentation.

In this paper, a meta-heuristic optimization region-based Chan–Vese (RCV) model is used to identify the suitable chamber border of ultrasound fetal image in the clinical settings. We proposed a new hybrid meta-heuristic algorithm integrating the CAT swarm and flower pollination algorithms to rectify the improper initial contour problem. In the hybrid method, the global pollination step of the flower pollination algorithm (FPA) is used for improving the distance averaging of the CATS algorithm. This newly proposed approach can also save the curvatures and border of the image showing structure overlapping, poor contrast, and high noise.

The contribution of the proposed method is as follows:

- A hybrid meta-heuristic algorithm is developed by combining CAT swarm and flower pollination algorithms. In the hybrid method, the distance averaging of the CAT algorithm is improved by flower pollination algorithm-based global pollination step.
- The proposed global pollination-based CAT swarm (GPCATS)-based Chan–Vese model is to utilize a hybrid meta-heuristic algorithm to provide an advantage to more effectively control the evolvement of the contour.

- Anatomical structure segmentation in fetal ultrasound sequences is done by our proposed GPCATS-based Chan–Vese model.

The outline of the remainder of the paper is as follows: In Sect. 2, the overview of the Chan–Vese model and proposed GPCATS optimizer are discussed. Section 3 describes the results and discussion. The conclusion is summed up in Sect. 4.

2 Material and methods

2.1 Background information about the Chan–Vese model

In this section, we briefly explained the Chan–Vese model. For image segmentation, the Mumford–Shah functional [51] is followed by Chan and Vese [16, 34] to propose a popularly known region-based model. The current or the initial contour is denoted as C , and the image to be detected is indicated as Ω , respectively. The energy minimization using the Chan–Vese model is expressed as follows:

$$\begin{aligned} E(c_1, c_2, C) = & \lambda_1 \int_{\text{in}(C)} |\Omega - c_1|^2 dx dy \\ & + \lambda_2 \int_{\text{out}(C)} |\Omega - c_2|^2 dx dy + \mu \cdot L(C) \\ & + \nu \cdot A(C) \end{aligned} \quad (1)$$

Here, the average intensity inside and outside of C is denoted as c_1 and c_2 , the area inside C is indicated as $A(C)$, and the length of C is termed as $L(C)$.

The energy $E(\phi, c_1, c_2)$ was derived after introducing the level set method [8] with one-dimensional Dirac measure δ_0 , and the Heaviside function H is shown as follows:

$$\begin{aligned} E(\phi, c_1, c_2) = & \mu \int_{\Omega} \delta_0(\phi(x, y)) |\nabla \phi(x, y)| dx dy + \nu \int_{\Omega} H(\phi(x, y)) dx dy \\ & + \lambda_1 \int_{\Omega} |\Omega - c_1|^2 H(\phi(x, y)) dx dy \\ & + \lambda_2 \int_{\Omega} |\Omega - c_2|^2 H(\phi(x, y)) dx dy \end{aligned} \quad (2)$$

where

$$\begin{cases} C := \{(x, y) \in \Omega : \phi(x, y) = 0\} \\ \text{in}(C) := \{(x, y) \in \Omega : \phi(x, y) > 0\}, \quad H(z) = \begin{cases} 1, z \geq 0 \\ 0, z < 0 \end{cases} \\ \text{out}(C) := \{(x, y) \in \Omega : \phi(x, y) < 0\} \end{cases}$$

Equation (2) is solved using two steps. Energy $E(\phi, c_1, c_2)$ is minimized with respect to c_1 and c_2 keeping ϕ as fixed. Then, we obtained

$$c_1(\phi) = \frac{\int_{\Omega} \Omega(x, y) H(\phi(x, y)) dx dy}{\int_{\Omega} H(\phi(x, y)) dx dy} \quad (3)$$

$$c_2(\phi) = \frac{\int_{\Omega} \Omega(x, y) (1 - H(\phi(x, y))) dx dy}{\int_{\Omega} (1 - H(\phi(x, y))) dx dy} \quad (4)$$

Subsequently, the energy $E(\phi, c_1, c_2)$ is minimized with respect to ϕ keeping c_1 and c_2 fixed. Then, we obtained

$$\frac{\partial \phi}{\partial t} = \delta(t) \left[\mu \operatorname{div} \left(\frac{\nabla \phi}{|\nabla \phi|} \right) - \nu - \lambda_1 (u_0 - c_1)^2 + \lambda_2 (u_0 - c_2)^2 \right] \quad (5)$$

In many situations, the shocks and flat shapes have been produced using the evolving contour [8]. The level set function is reinitialized periodically to the signed distance function till reaching its zero level set. This re-initialization process is done to solve the shocks and flat shapes creation in the evolving contour, which can be performed using the below step:

$$\frac{\partial \phi}{\partial t} = \operatorname{sign}(\phi_0) (1 - |\nabla \phi|) \quad (6)$$

where $\operatorname{sign}(\phi_0)$ denotes the sign function and ϕ_0 is the function to be re-initialized.

In discrete Eqs. (3) and (4), hence, we have used digital images throughout our approach. The discrete form of Eq. (3) is as follows:

$$c_1(\phi) = \frac{\sum_{\Omega} \sum_{\Omega} \Omega(x, y) H(\phi(x, y))}{\sum_{\Omega} \sum_{\Omega} H(\phi(x, y))} \quad (7)$$

$$c_2(\phi) = \frac{\sum_{\Omega} \sum_{\Omega} \Omega(x, y) (1 - H(\phi(x, y)))}{\sum_{\Omega} \sum_{\Omega} (1 - H(\phi(x, y)))} \quad (8)$$

In order to discrete the Eq. (4) in ϕ , a finite differences implicit scheme [16] is used by the Chan and Vese model. The steps used for implementing the Chan–Vese model are as follows: Initialize ϕ ; using Eq. (5), $c_1(\phi)$ and $c_2(\phi)$ are computed; to obtain a new ϕ from Eq. (4), the partial differential equation should be solved. Further, to continue or to stop the above steps, it is important to verify whether the solution is fixed (stationary) or not.

2.2 Formulation of GPCATS optimizer

2.2.1 Flower pollination algorithm

The biological flower pollination process inspired Yang for the development of flower pollination algorithm (FPA). Global pollination and local pollination are the two main steps involved in FPA. The four pollination rules stated in FPA are as follows [52]:

- (1) Global pollination is considered as a biotic cross-pollination, and the pollinators (e.g., insects) are responsible for transferring the pollen grains and moving in a way obeying Levy flights.
- (2) Local pollination occurs through self-pollination, and it is considered as abiotic pollination.
- (3) Flower constancy is developed by the pollinators, and its reproduction probability is directly proportional to the resemblance of two flowers.
- (4) Using a switching probability $S_p \in [0, 1]$, it is easy to control the switching or interaction between the local and global pollinations.

In the global pollination step, pollen grains of flowering plants are transported by the pollinators (e.g., insects). Insects carrying the pollens can fly often and move to a long distance. This allows for the reproduction of the fittest g^* by means of ensuring the pollination. The numerical expression for the first rule plus flower constancy is shown as follows:

$$X_i^{t+1} = X_i^t + \eta L(\lambda)(g^* - X_i^t) \quad (9)$$

In Eq. (9), X_i^t represents the pollen I; in other words, X_i^t is a solution vector at iteration t , g^* is the best-found solution at iteration t , η represents the step size scaling factor, and L is the pollination strength or the step size. The insect's long moves can be mimicked using Levy flight [52]. For this reason, the step size L is derived from the Levy distribution. λ is a constant that characterizes the flying angle.

2.2.2 CAT swarm optimization

The specific characteristic features of a cat's behaviour are identified to model the cat swarm optimization algorithm [53, 54]. Seeking mode and tracing mode are the two essential features termed from the cat's behaviour. Hence, the CAT swarm optimization (CSO) operation includes two modes. Depending on the mixture ratio (MR), the distribution of cats is done to the two modes.

SM In seeking mode, the parameters such as count of dimensions to change (CDC), seeking range dimension (SRD), and seeking memory pool (SMP) can largely affect the behaviour of cats. The number of duplicate cats is indicated using SMP, the dimensions required to be mutated are indicated using CDC (i.e., N and within the range of $[0, 1]$), and the modified value of the chosen dimensions are specified using SRD.

The step involved in seeking mode operation for j th cat is described as follows:

- (i) Create SMP number of copies of j th cat.
- (ii) For each copy (k th cat, $k = 1, 2, \dots, \text{SMP}$), change the position as follows:

$$X_k^t = \begin{cases} [1 + (2 \times \text{rand} - 1)] \times X_j^t, & \text{if } D \in N \\ X_j^t, & \text{otherwise} \end{cases} \quad (10)$$

- (iii) Calculate fitness values for all copies and select best fitness value (X_{best}^t) of the cat.
- (iv) Replace (X_j^t) with (X_{best}^t) if (X_j^t) is worse than (X_{best}^t) in terms of fitness value.

TM The tracing mode of CSO and the local searching ability of the swarm in particle swarm optimization (PSO) look similar. The cats in this mode changed their positions quickly to trace the targets. Hence, more energy is required by the cats to reach the targets. The steps of the tracing mode are described below:

The velocity of the i th cat is updated as follows:

$$V_j^{t+1} = w \times V_j^t + r_1 \times c_1 \times (X_{\text{best}}^t - X_j^t) \quad (11)$$

where the acceleration constant is denoted as c_1 , the inertia weight is indicated as w , and the global best position of the cat in t th iteration is represented as X_{best}^t and r_1 is a random value in the range $[0, 1]$.

The position of the i th cat is updated as follows:

$$X_j^{t+1} = X_j^t + V_j^{t+1} \quad (12)$$

Based on the MR, the updated cats are redistributed randomly in SM and TM if not the desired solutions are not attained while on completing the parallel procedures of both the SM and TM. The random redistribution process is continued until the desired solution is achieved.

2.2.3 Proposed GPCATS optimizer

Modified position-updated equation in tracing mode The tracing cat groups work the same as that of the PSO algorithm. The position of the cat is updated continuously using the current position information and the cat's own speed. Thus, each individual can move closer to the global optimal solution [55–57]. However, premature convergence is the main inadequacy found even after realizing the search of the global optimal solution. In the current trend, studying the position-updated equation in tracing mode (TM) can improve the cat swarm optimizer performance. In this research, the global pollination step of FPA is augmented with CAT swarm optimizer to enhance the global optima. In order to support the search of candidate individuals, the information belonging to another individual is used by this optimizer. The newly modified position-updated equation is indicated in Eq. (13)

$$X^{t+1} = \left(X_j^t + V_j^t \right) + \eta L(\lambda) \left(g^* - \left(X_j^t + V_j^t \right) \right) \quad (13)$$

Here, the step size $L(\lambda)$ wholly depends on the strength of the pollination following the Levy flights. The step size is controlled using the scaling factor η . The current best solution determined at the current iteration is defined as g^* . Different step size is used to cover the long distance, and this performance can be mimicked effectively using a Levy flight. Explicitly, $L > 0$ from a Levy distribution.

SM The SM process of classical CSO and GPCATS optimizer appears the same, and they are left unchanged. The updated cats are shifted to the corresponding modes depending on their flags where this process is performed if found, while after completing the parallel process of SM and TM, it is impossible to achieve the desired solution so far. Hence, this process is repeated until the desired solution is attained.

Algorithm description of GPCATS optimizer

- (1) Initialize a finite number of cats in D dimensional solution space randomly.
- (2) Initialize the velocity of the cats.
- (3) The best fitness cat is selected through computing the fitness value of each cat. In memory, the corresponding cat position is stored as X_{gbest} .
- (4) Cats are moved to the seeking mode based on MR, and the tracing mode of the cats is modified with respect to their flags.
- (5) Compute the fitness of each modified cat on completing the seeking and tracing mode. Then, the position of the best cat is stored $X_{I,j}$.

- (6) Compare with the fitness of X_{gbest} and $X_{I,j}$ and update X_{gbest} with the best position.
- (7) Stop the execution after achieving the desired solution; otherwise, in the corresponding modes, the updated cats continue its process and repeat the steps from 4 to 7.

Figure 2 depicts the flowchart of the proposed global pollination step size-based CAT swarm optimizer algorithm.

2.3 The proposed model: GPCATS-based Chan–Vese algorithm

Based on the procedures of the level set method, curve evolvement, and GPCATS, we formulated the GPCATS-based Chan–Vese algorithm to perform image segmentation. GPCATS is a population-based metaheuristic optimization algorithm, and this algorithm when integrated on the Chan–Vese algorithm used many initial contours at the same time. Conversely, a single initial contour is used by the traditional Chan–Vese algorithm. To find the best segmentation solution, the initial contours (cats) are iterated through adopting the curve evolution and level sets method. For the Chan–Vese algorithm, the global minimum energy function is provided by means of searching the optimum initial contour using GPCATS. The solutions will stuck into a local minimum due to the improper initial contours selection, but this will not be the case in our proposed GPCATS-based Chan–Vese algorithm because of its robustness in initial contour selection. The procedures of our proposed algorithm are explained as follows:

Initially, some initial seed points are generated randomly for each contour in the image. An initial contour making use of these seed points for each agent is represented through drawing a polygon. Considering the agents of GPCATS are the seed points of these contours; then, the energy function can be minimized by allowing the contours to be iterated repeatedly. Followed by this, for each initial contour, the fitness value is computed against every run of the GPCATS and based on the fitness values, the seed points are updated. Therefore, initial contours are adapted to the optimum by the algorithm. Hence, for curve evolution, the algorithm requires only minimum number of iterations. The desired segmentation result is attained in the last iteration of the algorithm.

The pseudocode of the GPCATS-based Chan–Vese model is given in Algorithm 1.

Proposed GPCATS with Chan-Vese Model

Step 1

1. a) Initialize the number of cats (solutions) N and the dimension D of the search space.
2. b) Initialize the lower and upper limits down and up in every D of the search space.
3. c) Initialize number of contour points K on the curve.
4. d) Initialize the position of cats x in the search space, randomly. (x is the vector size of K)
5. e) Initialize the constants.
6. f) Initialize the total number of GPCATS iterations T .
7. g) Initialize the total number contour evolutions S .
8. h) Construct an initial level set function for each cat using the seed positions of x .
9. i) Set iteration=1:

Step 2

10. **For** iteration=1 to maximum iteration (GPCATS iteration)
11. **For** $i=1$ to N
 - a) Check the search space boundaries of the cats.
 - b) Segment the given image by using the level set function as follows:
 14. **For** $n=0$ to S
 15. (i) Calculate the average intensities inside and outside the level set by using equation 3 and 4.
 16. (ii) Evolve the level set ϕ by solving the PDE using equation 5.
 17. (iii) Reinitialize $(\phi_{i,j}^{n+1})_i$ to be the signed distance function to $\{(\phi_{i,j}^{n+1})_i = 0\}$ by using equation 6.
 18. **End For**
 19. **End For**
 20. **For** $a=1$ to N (Evaluation of cats)
 21. Evaluate the objective function f for a i^{th} cat.
 22. **End For**
 23. Fitness evaluation of cats: Find the minimum objective value f_i^{\min} attained by each i^{th} cat till now.
 24. Update cat positions using equations (13) for all contour points.
 25. **End For**

Step 3

26. Report X_{gbest} as the best solution.

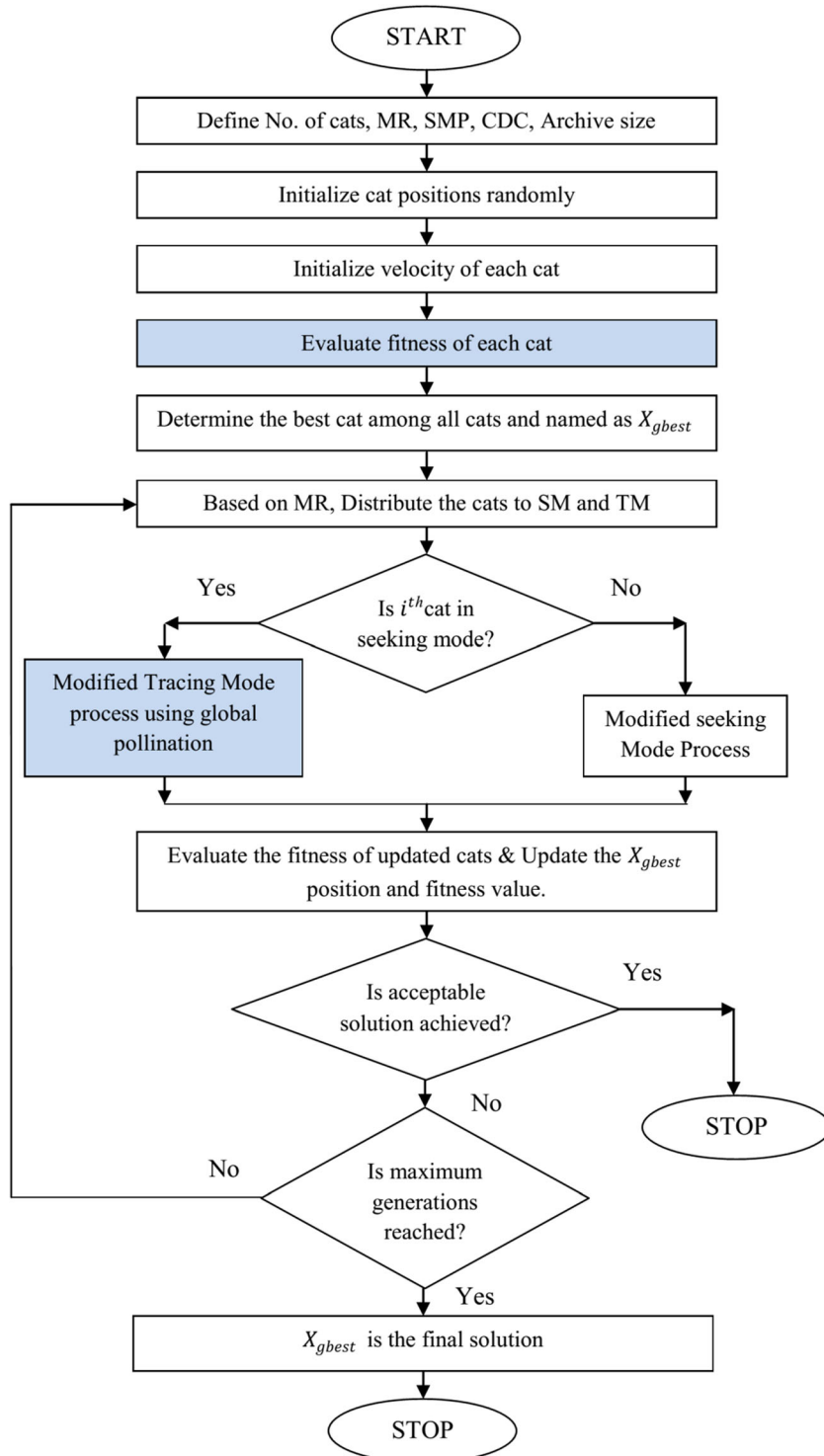


Fig. 2 Flowchart of the global pollination step size-based CAT swarm optimizer

3 Results

Experimental data The GPCATS-based robust Chan–Vese model has been implemented for several

ultrasound videos, and extensive experimental investigations and analyses of the results obtained are carried out, as discussed next. We required a dataset of some ultrasound videos of the fetal heart drawn from

12 subjects during routine clinical scans using a GE Voluson E8 ultrasound device. In a magnification and orientation range, the healthy fetal heart image is captured by the videos, though with the heart taking up approximately 30% or more of the image. The demographics of the cases are provided in Table 1. The gestational ages may range from 20 to 35 weeks. Each frame of each video was manually annotated according to the criteria shown in Fig. 1 in order to provide labels for training and validating the model. These annotations were approved by a clinician experienced in interpreting ultrasound videos of the fetal heart.

Quantitative evaluation is done to analyze the segmentation performance where a comparison between the manually segmented image (MSI) and automatically segmented image (ASI) is carried out. Similarity among both is expressed in terms of segmentation performance measure (SPM), expressed in percentage. The common metric of dice coefficient and the SPM computed in our implementations appears the same. Equation (14) is used to compute the SPM. Notably, the maximum possible value of SPM is 100% since the value of SPM should be as high as possible. Some of the well-known performance metrics such as true positive (TP), true negative (TN), false positive (FP), and false negative (FN) were used for evaluating the performance of our proposed method. Comparison between ASI image matrix and MSI image matrix is done to calculate these metrics. TP represents the number of pixels matched within the object region or the number of true positive pixels. TN indicates the number of pixels matched within the background region or the number of true negative pixels, FP indicates the number of pixels incorrectly matched within the object region or the number of false positive pixels, and FN represents the number of pixels incorrectly matched within the background region or the number of false negative pixels.

The sum of the metrics TP and TN results in the correctly marked pixel or CMP; conversely, the sum of the metrics FP and FN results in the incorrectly marked pixel or IMP metric.

$$SPM = \frac{[2 \times (ASI \cap MSI)]}{[|ASI| + |MSI|]} \quad (14)$$

Our proposed model should prove its efficiency on the local minima problem. Thus, to provide more satisfactory results, the Chan–Vese algorithm is provided with suitable test images; as they are selected because the algorithm requires better initial contours to generate accurate results. During energy minimization, the contour can trap within the first local minimum itself and also converging the deep concavities turns to be a difficult task. In such problems, the performance of our proposed model can be improved by applying only the selected suitable test images. Based on these criteria, to the test runs, the images having unfavorable features such as concavities, inhomogeneity in regions, or the improperly covered contour object boundaries have been selected.

In our experiments, for the regularized Dirac function, the parameter $\epsilon = 1$ is selected. Conversely, for numerical algorithms, the parameters (time step) $\Delta t = 1$ and (space step) $h = 1$ are selected. After conducting various experimental validations on these images, we observed the fact from the obtained results that the traditional conventional Chan–Vese model determined the value 200 as the optimal number of iteration required for contour evolution. The reason for the determination of value 200 as the optimal number of iterations is that, when experimental runs are done below 200 iterations, it is impossible to complete the whole convergence process of the contour. Also, any of the significant changes in the contour evolutions are not found ideally for more than 200 iterations.

Similarly, the value 50 was determined as the optimal number of iteration required for contour evolution (S in Algorithm 2) in our proposed GPCATS-based Chan–Vese model. Subsequently, the value 3 was determined as the total number of iterations of the model (T in Algorithm 2) for achieving the computational efficiency. These values are found to be enough for avoiding the solutions sticking within the local minima points. We can ensure that our proposed model incurs only 75% less number of iterations for contour to converge compared to the iteration numbers required by the conventional Chan–Vese model. Our GPCATS-based Chan–Vese model requires only 50 numbers of iterations while the Chan–Vese model requires 200 numbers of iterations to converge. But a slight increase

Table 1 Demographic characteristics of the study samples

Characteristics	Overall Mean (standard deviation)
Age (years)	30.25 (8.15)
Gestational age (weeks)	27.04 (2.04)
Body mass index (kg/m^2)	30.65 (7.44)

in execution time is identified with GPCATS-based Chan–Vese model because to avoid local minima during energy minimization and for optimizing the contour seed point, the contour evolution is repeated three times for convergence.

Using different types of contours, the Chan–Vese algorithm was tested on four videos and the results obtained are compared with the segmentation results of the GPCATS-based Chan–Vese model. Figures 3, 4, 5, and 6 depict the test results obtained for each image using the Chan–Vese algorithm, whereas the yellow indicating the initial contours (polygons) is in the first row and the magenta color indicating obtained final contours is in the second row. From the figures (Figs. 3, 4, 5, and 6), we observed that the successful segmentation results are obtained on the first initial contour and the images are not segmented on the last three initial contours.

The images having boundary concavities, background clutter, and inhomogeneous regions are not so much easy to handle by the conventional Chan–Vese model. The situation for the appearance of inhomogeneous regions problem in the background is shown in Fig. 3. From Fig. 3, it can be observed that only for a certain limit the segmentation is possible to be satisfied with this kind of images. This is because, the inhomogeneity regions of the background are

covered less or not covered (since it is a region-based model) or selecting the initial contour nearer to the object boundaries. Thus, it is more significant to provide importance for the selection of initial contours, particularly for this case. During the energy minimization of the Chan–Vese model, the solutions will stick into the first local minimum itself due to the presence of non-convexity in the energy function. That is why the poor results are obtained for the initial contours which are far away from the object boundaries as demonstrated in Figs. 4, 5, and 6. In other words, before converging to the global minima, the contours are trapped within the first local minima of the energy minimization. Figure 7 presents the segmentation results in different iterations such as 5, 10, and 20 for three images.

For each test image in the GPCATS-based Chan–Vese model, the test runs have been performed for 30 times using the randomly generated initial contours. Figure 8 indicates the five of these test runs. The results obtained have ensured the reliability and robustness of the GPCATS-based Chan–Vese model by means of satisfying the segmentation not allowing the solutions to stick in the local minima and also in handling the same test images. For each contour initialization considered, the number of iterations incurred for the corresponding evolutions of the fitness function

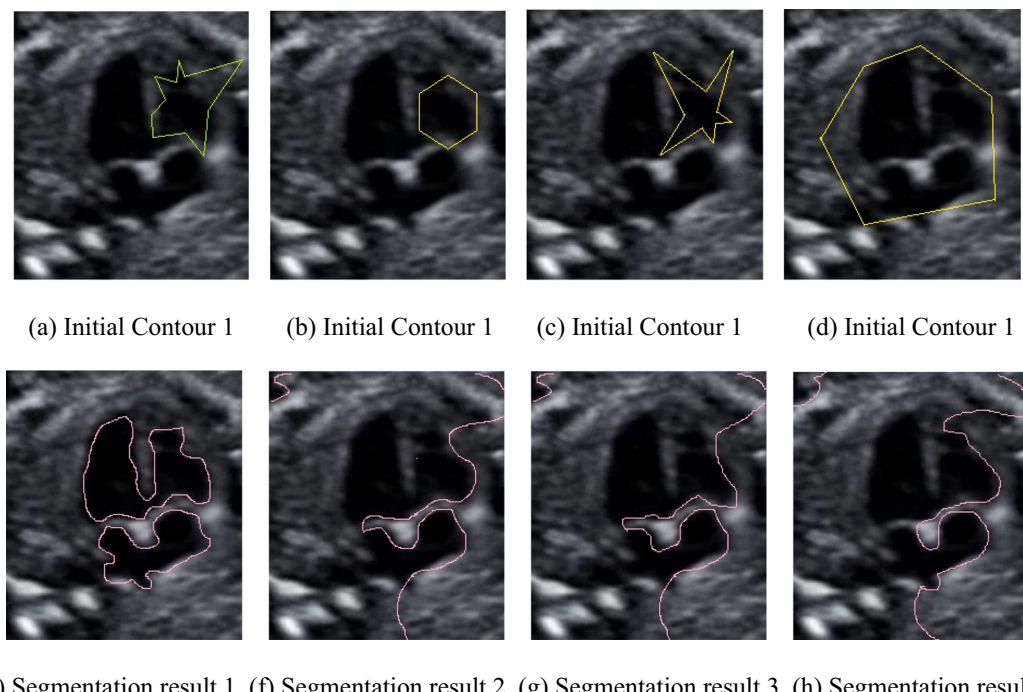


Fig. 3 Performance of the Chan–Vese algorithm for the Image 1 (Frame 24.png). First row displays the positions of the initialization contours and the second row displays the segmentation outcomes, respectively. **a** Initial contour 1. **b** Initial contour 1. **c** Initial contour 1. **d** Initial contour 1. **e** Segmentation result 1. **f** Segmentation result 2. **g** Segmentation result 3. **h** Segmentation result 4

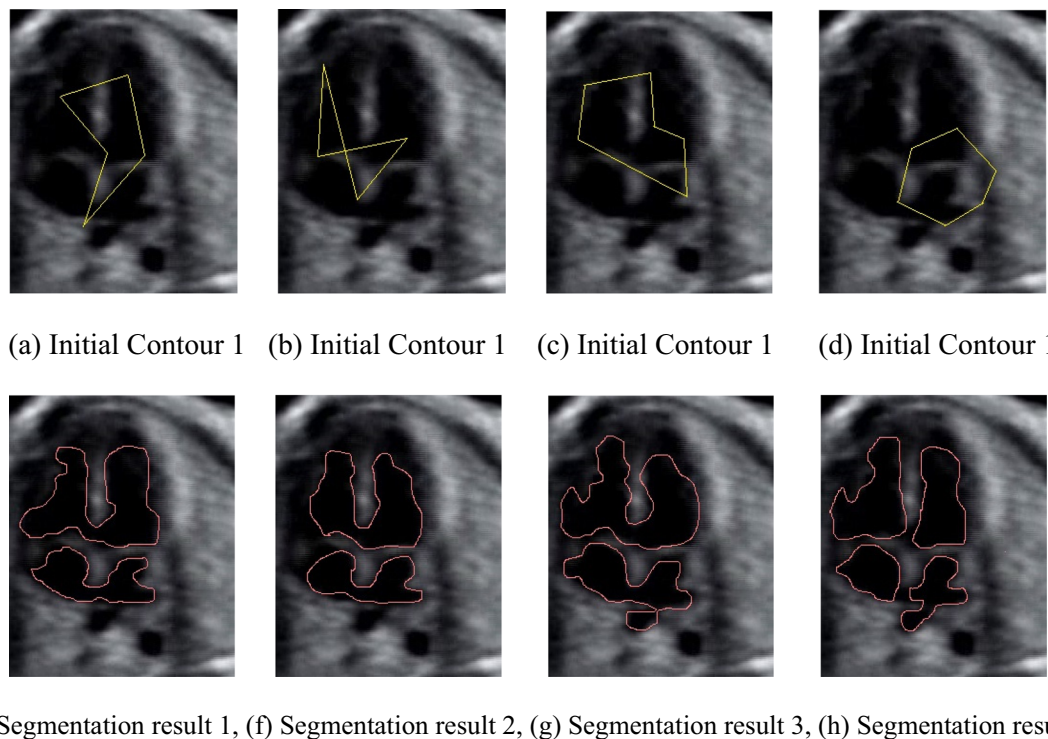


Fig. 4 Performance of the Chan–Vese algorithm for the Image 2 (Frame 54.png). First row displays the positions of the initialization contours and the second row displays the segmentation outcomes, respectively. **a** Initial contour 1. **b** Initial contour 1. **c** Initial contour 1. **d** Initial contour 1. **e** Segmentation result 1. **f** Segmentation result 2. **g** Segmentation result 3. **h** Segmentation result 4

Fig. 4 Performance of the Chan–Vese algorithm for the Image 2 (Frame 54.png). First row displays the positions of the initialization contours and the second row displays the segmentation outcomes, respectively. **a** Initial

contour 1. **b** Initial contour 1. **c** Initial contour 1. **d** Initial contour 1. **e** Segmentation result 1. **f** Segmentation result 2. **g** Segmentation result 3. **h** Segmentation result 4

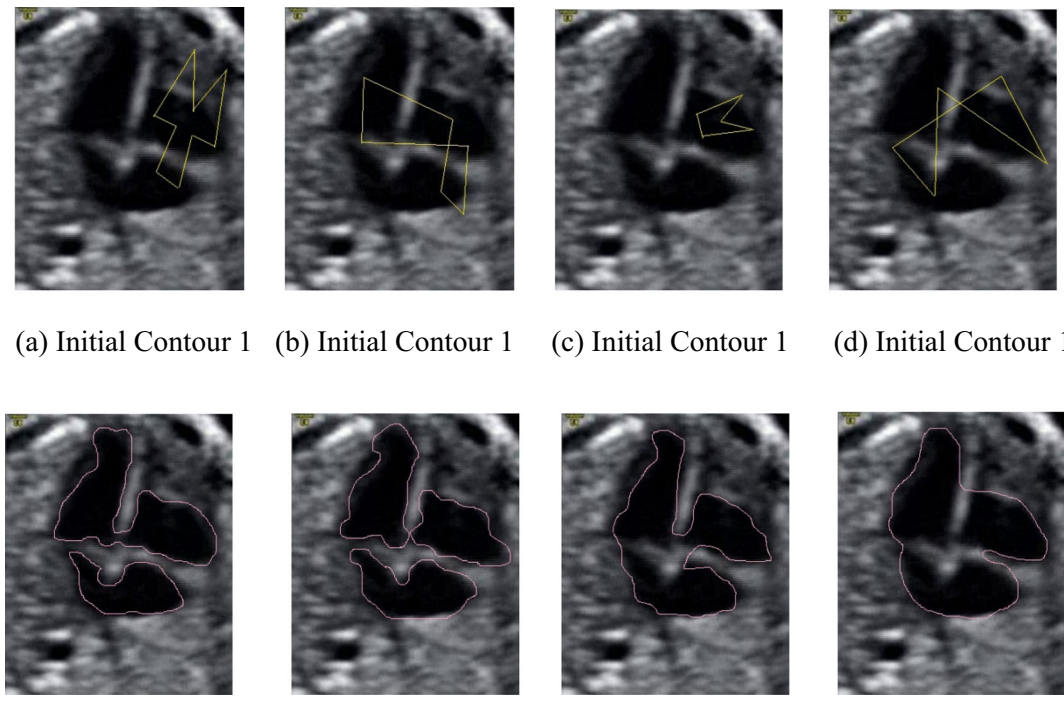


Fig. 5 Performance of the Chan–Vese algorithm for the Image 3 (Frame 48.png). First row displays the positions of the initialization contours and the second row displays the segmentation outcomes, respectively. **a** Initial contour 1. **b** Initial contour 1. **c** Initial contour 1. **d** Initial contour 1. **e** Segmentation result 1. **f** Segmentation result 2. **g** Segmentation result 3. **h** Segmentation result 4

Fig. 5 Performance of the Chan–Vese algorithm for the Image 3 (Frame 48.png). First row displays the positions of the initialization contours and the second row displays the segmentation outcomes, respectively. **a** Initial

contour 1. **b** Initial contour 1. **c** Initial contour 1. **d** Initial contour 1. **e** Segmentation result 1. **f** Segmentation result 2. **g** Segmentation result 3. **h** Segmentation result 4

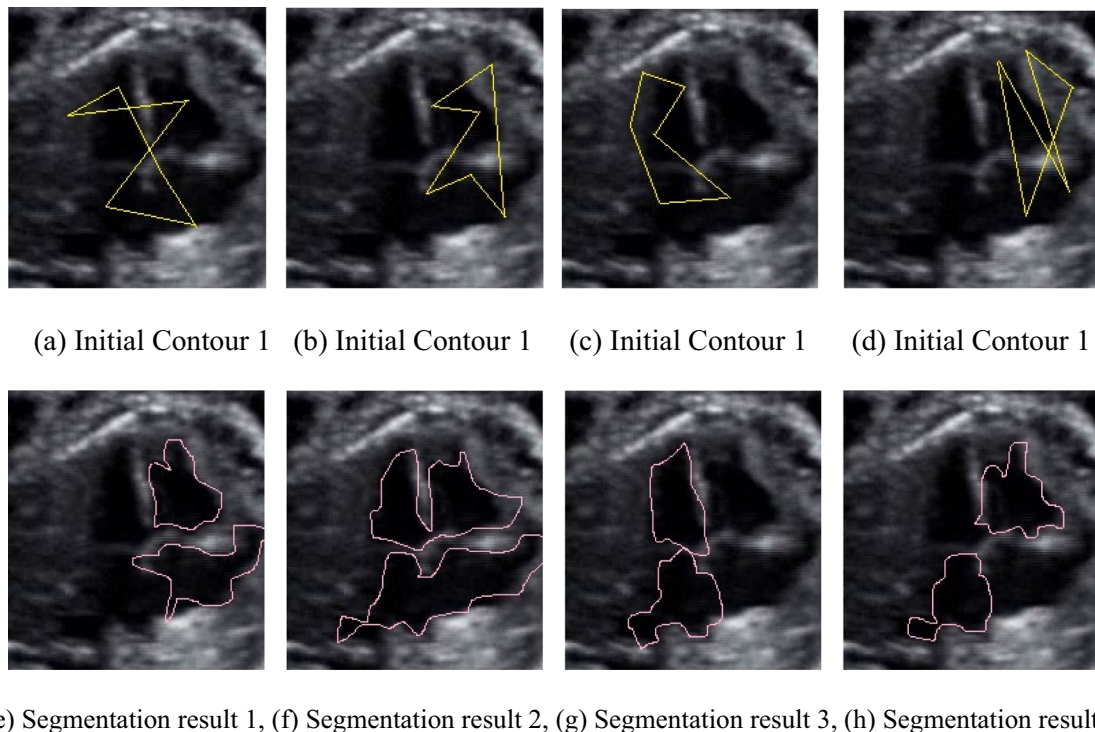


Fig. 6 Performance of the Chan–Vese algorithm for the Image 4 (Frame 35.png). First row displays the positions of the initialization contours and the second row displays the segmentation outcomes, respectively. **a** Initial contour 1. **b** Initial contour 1. **c** Initial contour 1. **d** Initial contour 1. **e** Segmentation result 1. **f** Segmentation result 2. **g** Segmentation result 3. **h** Segmentation result 4

energy is shown in Fig. 9a. However, from the results, it can be observed that the fitness function energy reached closer to the global minimum while on selecting the initial contour 2. Conversely, for all other iterations, the energy function is not improved with other four situations. The similar fitness function energy plot for GPCATS-based Chan–Vese model obtained with a number of iterations is shown in Fig. 9b. For all curves in Fig. 9b, our proposed algorithm reached close to the global minimum specifically for all initial contour choices. From this, we can ensure that better segmentation performance is achieved with our proposed algorithm and remains invariant with initial contours choices.

The number of iterations incurred for the corresponding evolutions of the fitness function energy is shown in Fig. 10. However, from the results, it can be observed that the fitness function energy reached somewhat closer to the global minimum while on selecting the initial contour 4. Figure 10a, b depicts that our proposed robust algorithm was employed for five test run cases. The results obtained even for these cases too indicated better segmentation results on using our GPCATS-based algorithm for any random selection of the initial contour.

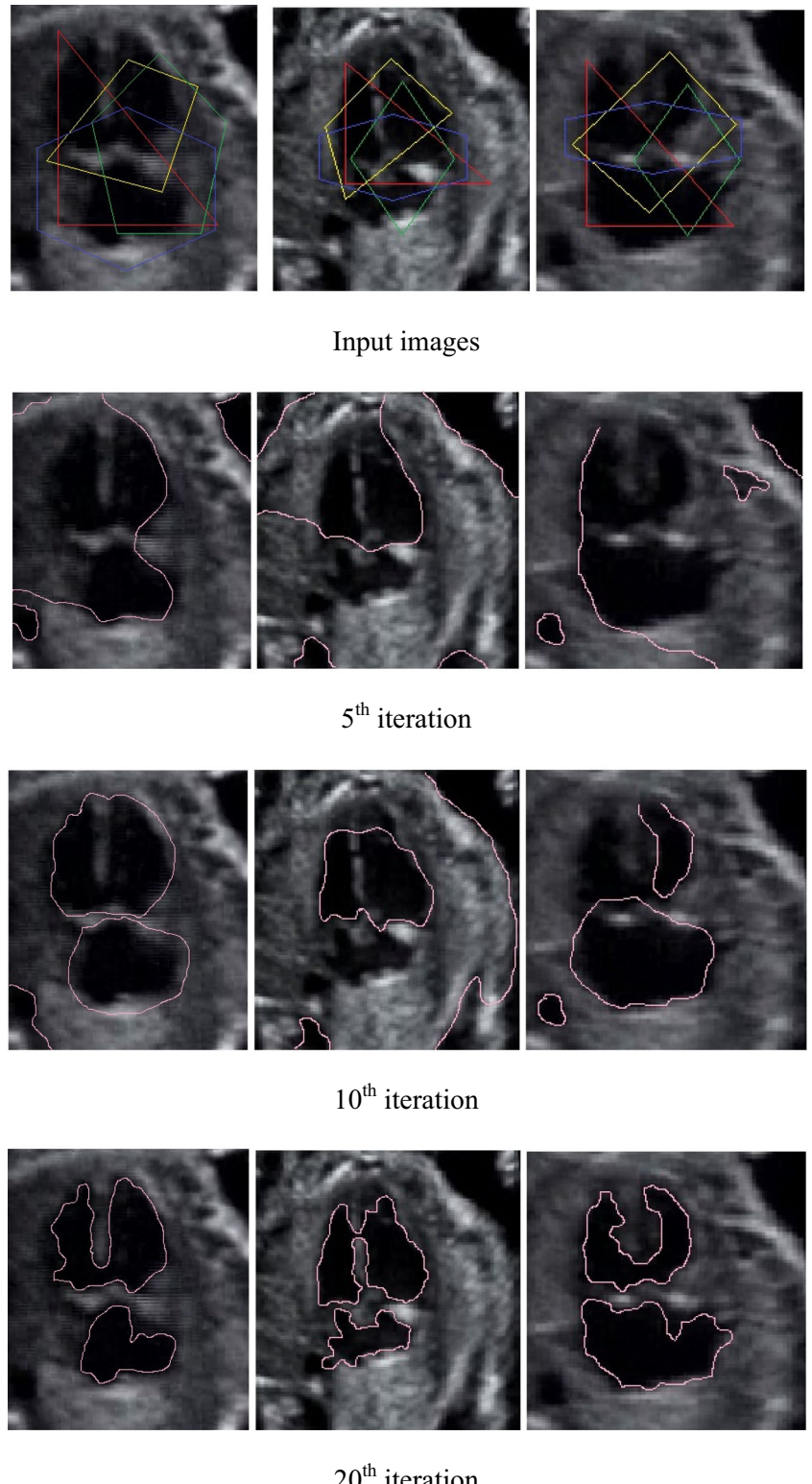
Figure 11 depicts the convergence characteristics of the GPCATS, CATS, and CSO algorithms. Compared to

contour 1. **b** Initial contour 1. **c** Initial contour 1. **d** Initial contour 1. **e** Segmentation result 1. **f** Segmentation result 2. **g** Segmentation result 3. **h** Segmentation result 4

the CATS and PSO algorithms, the GPCATS exhibited better convergence performance. The segmentation performance results obtained by comparing our proposed system and the conventional Chan and Vese algorithm are shown in Tables 2 and 3. The SPM value demonstrated in Table 2 indicated that the segmentation performance is good only with contour 4. Table 3 indicates that highly valuable segmentation performance is achieved with our proposed algorithm (i.e., SPM of more than 99.95%) for every five independent runs on various initial choices. According to Table 2, for most cases, the CMP metric is low and this is not the case for contour 4 because it has the ability to provide better segmentation performance. However, the CMP metric value is nearer enough to 100% for all cases as shown in Table 3. The tables also indicate the minimum fitness energy value attained using both the models. Contour 4 in the conventional Chan and Vese algorithm alone has the ability to reach closer to the global minimum value. According to the results depicted in Table 3, our proposed model can provide good segmentation performance with lower fitness functional energy encouraging then to reach the global minimum compared to the segmentation performance achieved with the conventional Chan and Vese algorithm.

Based on the system properties and image size, the time needed for segmentation is evaluated. Considering

Fig. 7 Segmentation results in different iterations. Row 1: original images, row 2: segmentation results at 5 iterations, row 3: segmentation results at 10 iterations, row 4: segmentation results at 20 iterations



all these criteria, a fair comparison has been made in terms of time complexity and a comparison of computational time on a system with 2.20 GHz CPU and 8 GB of RAM has been done. While it took 14.624 s

for the Chan–Vese model to locate the solution on image 1 (size = 300×225), it took 57.819 s for the GPCATS-based Chan–Vese model. Similar durations have been observed for other test images. Based on

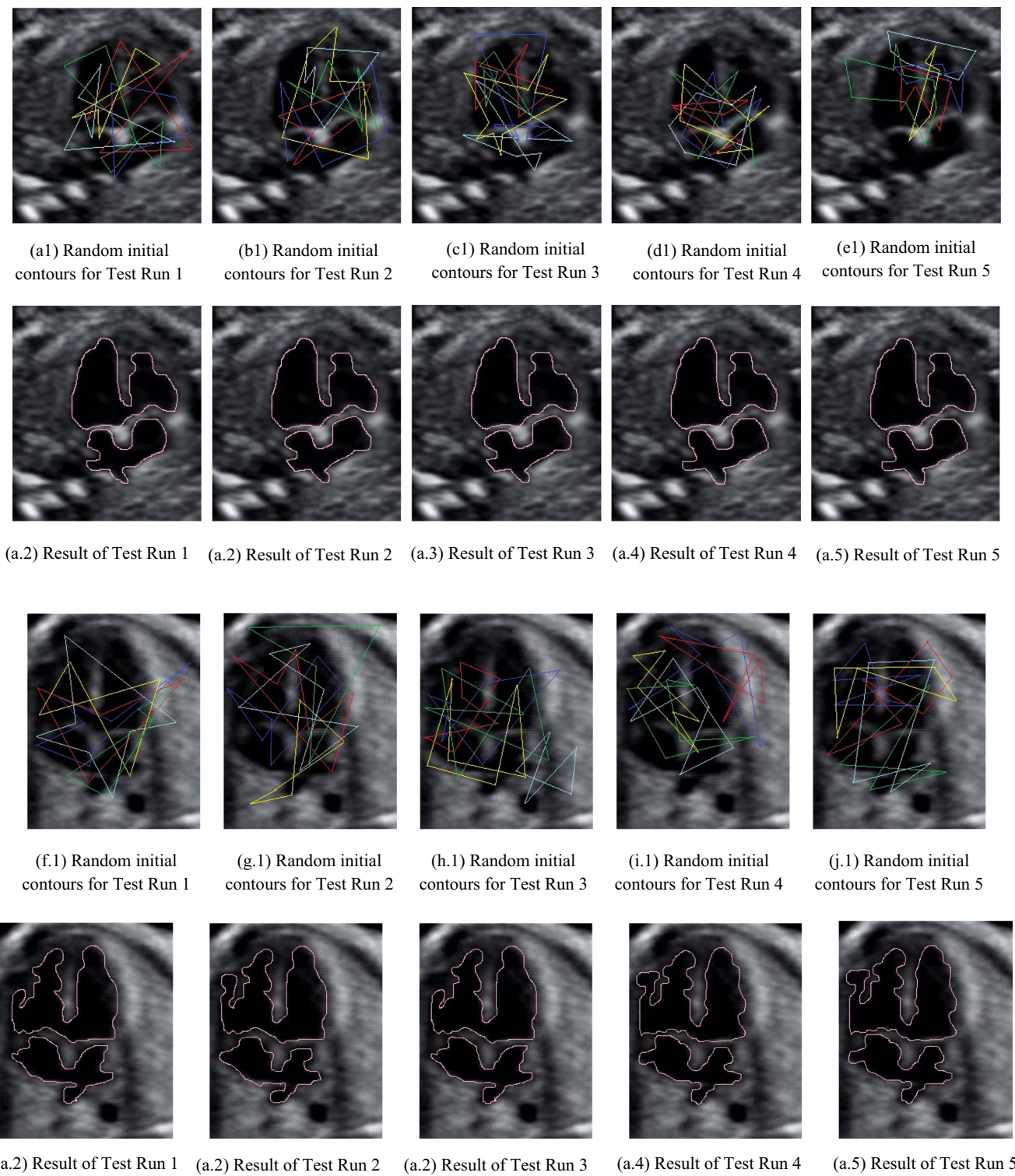
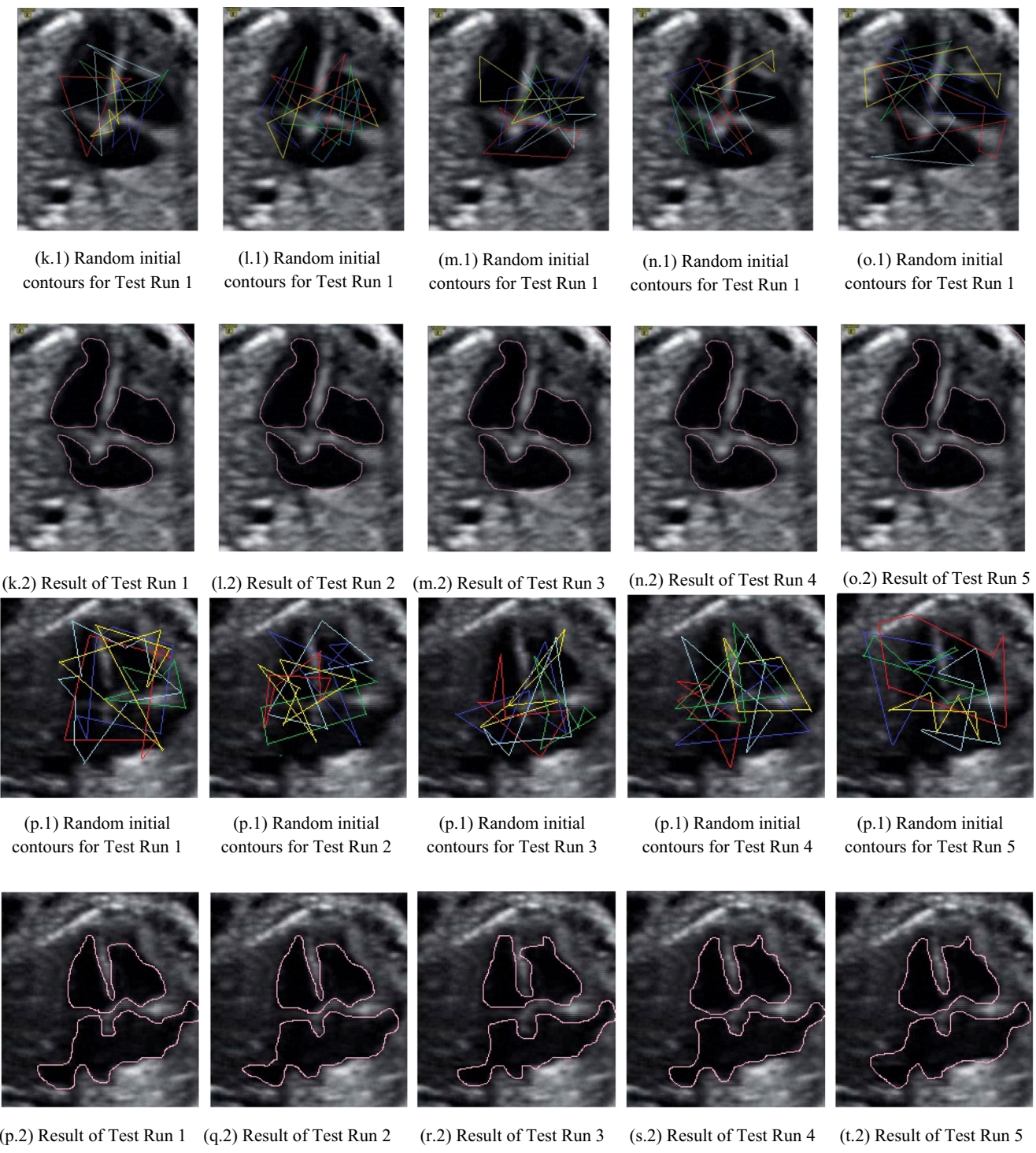


Fig. 8 Segmentation outcomes of our proposed GPCATS-based Chan–Vese model which provides good performance in each

the Chan–Vese algorithm, the running time is extended by our proposed algorithm which is most reliable and robust in handling the local minima problem. As same as that of the running time of many existing algorithms, it also has acceptable running times.

Comparison against other methods Furthermore, to assess the superiority of the proposed segmentation method, their results were compared with the following segmentation methods:

**Fig. 8** (continued)

Method 1: Geodesic active contour (GAC) method as described in [19].

Method 2: Active contour is driven by region-scalable fitting (ACMRSF) model as described in [16, 17].

Method 3: The region-based active contour model with spatial FCM (RBACM-SFCM) as described in [58].

Method 4: The edge-based active contour model using the level set method (EBACM) as described in [18].

Furthermore, the Hausdorff distance is evaluated for each ultrasound image segmented with all the aforementioned methods. Table 4 illustrates the averaged Hausdorff distance

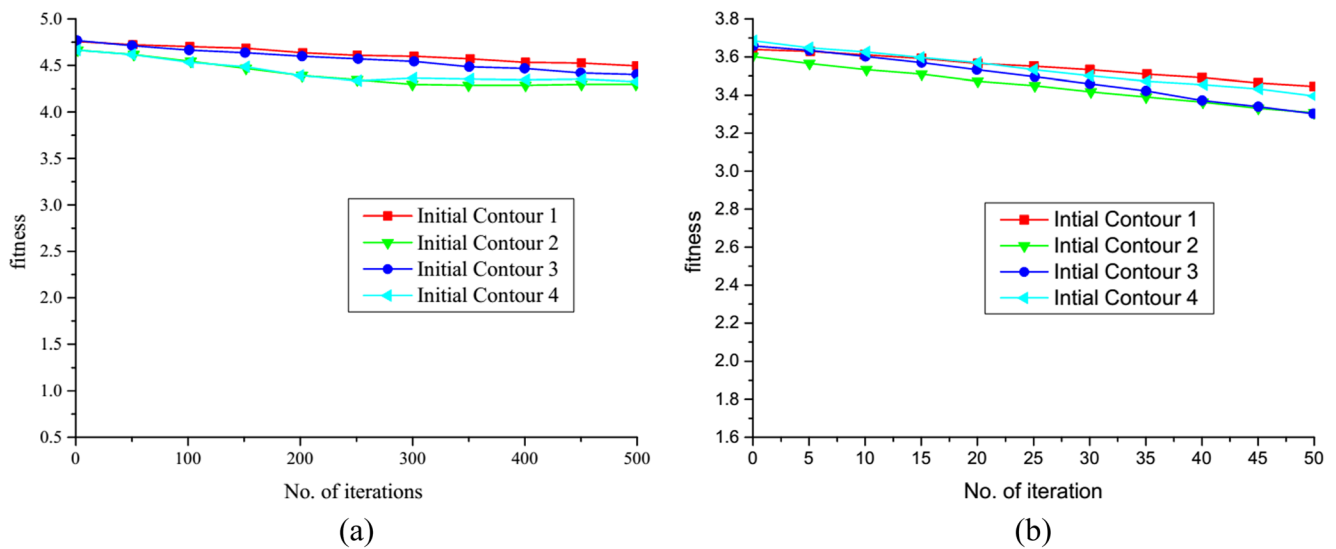


Fig. 9 The variation of the fitness function energy with the number of iterations for **a** image 1 and **b** image 2

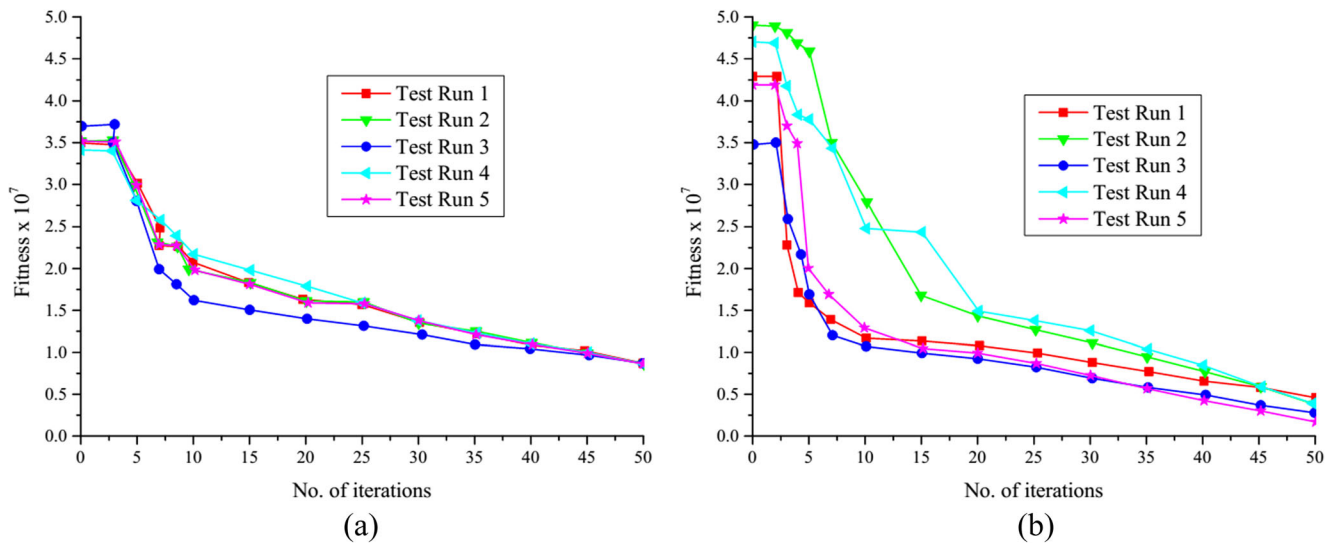


Fig. 10 The variation of the fitness function energy with the number of iterations for the **a** image 1 and **b** image 2

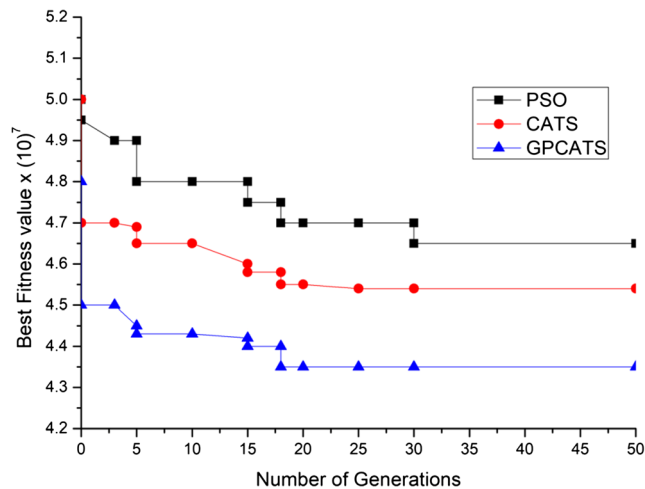


Fig. 11 Convergence plot of the fitness value using GPCATS, CATS, and PSO

Table 2 The segmentation performance of conventional Chan and Vese algorithm for different images (frames)

	Initial contour	SPM (%)	CMP (%)	IMP (%)	TP (%)	TN (%)	FP (%)	FN (%)
Image 1 (Frame 24.png)	1	26.957	96.7	2.98	0.00	35.70	32.78	27.22
	2	27.989	90.9	12.45	0.00	22.15	33.74	32.34
	3	65.978	92.1	10.65	20.15	32.25	32.60	27.98
	4	96.244	94.6	1.71	22.19	42.62	32.10	14.64
Image 2 (Frame 54.png)	1	68.949	93.0	0.43	30.14	40.12	4.86	0.62
	2	38.245	92.8	0.87	31.22	40.13	4.76	10.60
	3	93.214	90.3	0.65	32.56	42.44	4.62	0.98
	4	89.990	88.9	0.74	31.45	62.43	4.97	10.74
Image 3 (Frame 48.png)	1	98.929	70.2	2.81	0.00	63.13	30.81	22.94
	2	92.964	45.3	0.94	38.12	65.18	31.22	41.32
	3	99.951	38.7	5.80	30.64	62.10	25.74	30.78
	4	95.968	59.4	2.10	39.84	63.32	5.81	24.23
Image 4 (Frame 35.png)	1	98.922	46.5	0.4	34.57	64.20	0.89	12.87
	2	93.922	47.1	1.35	0.00	67.23	0.54	10.62
	3	98.924	88.4	4.23	17.87	66.42	0.76	10.48
	4	97.932	89.0	1.05	20.56	60.12	0.24	0.17

Table 3 The segmentation performance of our proposed algorithm for different images (frames)

	Initial contour	SPM (%)	CMP (%)	IMP (%)	TP (%)	TN (%)	FP (%)	FN (%)	Fitness reached ($\times 10^7$)
Image 1 (Frame 24.png)	1	99.957	98.7	0.47	0.00	45.68	32.78	20.13	1.247
	2	99.989	97.9	1.21	2.36	46.16	33.74	22.51	1.587
	3	99.978	99.1	1.06	20.15	44.20	32.60	17.98	1.765
	4	99.967	98.6	1.71	22.19	45.71	32.10	15.84	1.846
Image 2 (Frame 54.png)	1	99.949	99.0	0.43	30.14	42.16	4.86	0.22	4.654
	2	99.967	99.8	0.87	31.22	42.16	4.76	0.90	4.862
	3	99.974	99.3	0.65	32.56	43.12	4.62	0.17	5.236
	4	99.990	99.9	0.74	31.45	60.42	4.97	0.74	4.985
Image 3 (Frame 48.png)	1	99.929	98.2	2.81	36.10	62.13	30.81	12.94	6.987
	2	99.964	95.3	0.94	38.12	64.18	31.22	11.32	6.520
	3	99.951	98.7	5.80	30.64	61.10	25.74	10.78	6.871
	4	99.968	99.4	2.10	39.84	62.30	5.81	14.23	8.241
Image 4 (Frame 35.png)	1	99.991	96.5	0.4	34.57	68.21	0.89	0.87	6.227
	2	99.984	97.1	1.35	32.58	67.23	0.54	0.62	6.423
	3	99.996	98.4	4.23	37.87	66.42	0.76	0.48	6.721
	4	99.972	99.0	1.05	30.56	62.10	0.24	0.17	7.3651

Table 4 Comparative performance of the segmentation methods with the average and standard deviation (STD) of Hausdorff distance, average computation time, and average iterations

Methods	Hausdorff distance (AVG \pm SD)	Average computational time (s)	Average iterations
Method 1 [19]	6.9968 \pm 3.0892	140.251	1250
Method 2 [16, 17]	4.8474 \pm 1.4806	15.520	242
Method 3 [58]	4.3478 \pm 1.1638	2.521	86
Method 4 [18]	3.5788 \pm 1.3364	13.370	85
Proposed	2.5204 \pm 1.2503	2.102	20

metric (AVG \pm STD) attained by each method. It specifies the superiority of the proposed scheme with the smallest Hausdorff distance values. The computational time taken by all the segmentation techniques is also calculated. For such

comparative analysis, the averaged computational time in seconds and an average number of iterations taken by the individual approach are illustrated in Table 4. Lastly, from Table 4, it is also examined that the proposed approach takes a less

number of iterations and also does not take too much computation time as compared to other existing segmentation methods.

4 Conclusion

This study explained the development of an improved version of the RCV model for active contour-based image segmentation problems. We have formulated a new and hybrid meta-heuristic optimization algorithm namely global pollination-based CAT swarm (GPCATS) optimizer to solve the fitting energy minimization problem. In the GPCATS method, the global pollination step of the flower pollination algorithm (FPA) is used for improving the distance averaging of the CATS algorithm. RCV model implementation was done for two-phase level sets using the proposed algorithm, and the performance was analyzed on different fetal heart ultrasound videos acquired from 12 subjects. Experimental results of the proposed model proved that the precision of locating boundaries is improved greatly and requires only a reduced number of iterations (75% less) for convergence compared to the traditional RCV model. In the future, we intend to enhance this approach to a fully automated system. Hence, studying some processing operations on the image and generating an automatic region of interest will be helpful to improve the approach to a fully automated system.

Acknowledgments We thank our excellent radiological technician, Chennai, for his important input regarding the technical part of this study.

Compliance with ethical standards

This study was conducted with approval from the Ethics Committee of Thasiah Medical Centre, Tamilnadu, India. Written informed consent was obtained from all participants' guardians.

Conflict of interest The authors declare that they have no conflict of interest.

References

- Rueda S, Knight CL, Papageorghiou AT, Noble JA (2015) Feature-based fuzzy connectedness segmentation of ultrasound images with an object completion step. *Med Image Anal* 26:30–46
- Mitchell SC, Korones SB, Berendes HW (Mar 1971) Congenital heart disease in 56,109 births: incidence and natural history. *Circulation* 43(3):323–332
- Hoffman KL, Kaplan S (2002) The incidence of congenital heart disease. *J Am Coll Cardiol* 39:1890–1900
- Allan LD, Chita SK, Sharland GK, Fagg NL, Anderson RH, Crawford DC (1989) The accuracy of fetal echocardiography in the diagnosis of congenital heart disease. *Int J Cardiol* 25: 279–288
- Maraci MA, Bridge CP, Napolitano R, Papageorghiou A, Noble JA (2017) A framework for analysis of linear ultrasound videos to detect fetal presentation and heartbeat. *Med Image Anal* 37:22–36
- Vijayalakshmi S, Sriraam N, Suresh S, Muttan S (2013) Automated region mask for four-chamber fetal heart biometry. *J Clin Monit Comput* 27(2):205–209
- Becher R, Wegner RD (2006) Detailed screening for fetal anomalies and cardiac defects at the 11–13 week scan. *Ultrasound Obstet Gynecol* 27:613–618
- Osher S, Sethian JA (1988) Fronts propagating with curvature-dependent speed: algorithms based on Hamilton–Jacobi formulation. *J Comput Phys* 79:12–49
- Sarti A, Malladi R (1999) A geometric level set model for ultrasound image analysis, in Computing Sciences Directorate Mathematics Department. University of California, Berkeley, CA
- Lin N, Yu W, Duncan JS (2003) Combinative multi-scale level set framework for echocardiographic image segmentation. *Med Image Anal* 7(4):529–537
- Paragios N (2003) A level set approach for shape-driven segmentation and tracking of the left ventricle. *IEEE Trans Med Imaging* 22(6):773–776
- Chen Y, Huang F, Tagare HD, Murali R, Wilson D, Geiser EA (2003) Using prior shape and intensity profile in medical image segmentation, ICCV, pp. 1117–1124
- Sarti A, Malladi R, Sethian JA (2000) Subjective surfaces: a method for completion of missing boundaries. *PNAS* 12(97):6258–6263
- Corsi C, Borsari M, Sarti A, Lamberti C, Travaglini A, Shiota T, Thomas JD (2001) Left ventricular endocardial surface detection based on real time 3D echocardiographic data. *Eur J Ultrasound* 13: 41–51
- Corsi C, Saracino G, Sarti A, Lamberti C (2002) Left ventricular volume estimation for real-time-dimensional echocardiography. *IEEE Trans Med Imaging* 21:1202–1208
- Chan T, Vese LA (2001) Active contours without edges. *IEEE Trans Image Process* 10(2):266–277
- Chunming L, Chiu-Yen K, Gore JC, Zhaohua D (2008) Minimization of region-scalable fitting energy for image segmentation. *IEEE Trans Image Process* 17(10):1940–1949
- Chunming L, Chenyang X, Changfeng G, Fox MD (2010) Distance regularized level set evolution and its application to image segmentation. *IEEE Trans Image Process* 19(12):3243–3254
- Paragios N, Deriche R (2000) Geodesic active contours and level sets for the detection and tracking of moving objects. *IEEE Trans Pattern Anal Mach Intell* 22(3):266–280
- Cremers D, Sochen N, Schnorr C (2003) Towards recognition-based variational segmentation using shape priors and dynamic labeling. In L. Griffith, (ed) Int. Conf. on Scale Space Theories in Computer Vision, volume 2695 of LNCS:388–400, Isle of Skye. Springer
- Piccoli L, Dahmer A, Scharcanski J, Navaux P (1999) Fetal echocardiographic image segmentation using neural networks, In 7th Int Conf on Imag Proc Appl, volume 2, pages 507–511, Manchester
- Lassige T, Benkeser P, Fyfe D, Sharma S (2000) Comparison of septal defects in 2d and 3d echocardiography using active contour models. *Comput Med Imaging Graph* 24(6):377–388
- Siqueira M, Scharcanski J, Navaux P (2002) Echocardiographic image sequence segmentation and analysis using self-organizing maps. *J VLSI Signal Proc Syst Signal, Image, Video Technol* 32: 135–145

24. Dindoyal I, Lambrou T, Deng J, Todd-Pokropek A (2007) Level set snake algorithms on the fetal heart. IEEE International Symposium on Biomedical Imaging. p. 864–7
25. Chen Y, Tagare H, Thiruvenkadam S, Huang F, Wilson D, Gopinath K, Briggs R, Geiser E (2002) Using prior shapes in geometric active contours in a variational framework. *Int J Comput Vis* 50(3):315–328
26. Cremers D, Tischhauser F, Weickert J, Schnorr C (2002) Diffusion snakes: introducing statistical shape knowledge into the Mumford-Shah functional. *Int J Comput Vis* 50(3):295–313
27. Chen J, Zhang H, Zhang W, X D, Zhang Y, Li S (2018) Correlated regression feature learning for automated right ventricle segmentation. *IEEE J Transl Eng Health Med* 6:1–10
28. X D, Zhang W, Zhang H, Chen J, Zhang Y, JC Warrington G, Brahm SL (2018) Deep regression segmentation for cardiac biventricle MR images. *IEEE Access* 6:3828–3838
29. Zhang H, Gao Z, Xu L, Yu X, Wong KCL, Liu H, Zhuang L, Shi P (2018) A Meshfree representation for cardiac medical image computing. *IEEE J Transl Eng Health Med* 6:1–12
30. Z Gao Y, Li Y, Sun J, Yang H, Xiong H, Zhang X, Liu WW, Liang D, Li S (2018) Motion tracking of the carotid artery wall from ultrasound image sequences: a nonlinear state-space approach. *IEEE Trans Med Imaging* 37:273–283
31. Fong KW, Toi A, Salem S, Horberger LK, Chitayat D, Keating SJ, McAuliffe F, Johnson J-A (2004) Detection of fetal structural abnormalities with US during early pregnancy. *Radio Graphics* 24: 157–174
32. Lin N, Weichuan Y, Duncan JS (2002) Combinative multi-scale level set framework for echocardiographic image segmentation. Springer-Verlag, Berlin, MICCAI 2488, pp 682–689
33. Leventon ME, Grimson WEL, Faugeras O (2002) Statistical shape influence in geodesic active contours. In 5th IEEE EMBS International Summer School on Biomedical Imaging, IEEE, p 8
34. Li C, Xu C, Gui C, Fox MD (2010) Distance regularized level set evolution and its application to image segmentation. *IEEE Trans Image Process*, 19(12):3243–3254
35. Çataloluk H, Vehbi Çelebi F (2018) A novel hybrid model for two-phase image segmentation: GSA based Chan-Vese algorithm. *Eng Appl Artif Intell* 73:22–30
36. Santiago C, Marques JS, Nascimento JC (2013) A robust deformable model for 3D segmentation of the left ventricle from ultrasound data, mathematical methodologies in pattern recognition and machine learning. *Springer Proc* 30:163–178
37. Gupta D, Anand RS, Tyagi B (2015) A hybrid segmentation method based on Gaussian kernel fuzzy clustering and region based active contour model for ultrasound medical images. *Biomed Signal Process Control* 16:98–112
38. Yan JY, Zhuang T (Nov. 2003) Applying improved fast marching method to endocardial boundary detection in echocardiographic images. *Pattern Recogn Lett* 24(15):2777–2784
39. Mishra A, Dutta PK, Ghosh MK (2003) A GA based approach for boundary detection of left ventricle with echocardiographic image sequences. *Image Vis Comput* 21:967–976
40. Hunter I, Soraghan J, Christie J, Durrani T (1993) Detection of echocardiographic left ventricle boundaries using neural networks. *Comput Cardiol* 20:201–204
41. Malassiotis S, Strintzis MG (1999) Tracking the left ventricle in echocardiographic images by learning heart dynamics. *IEEE Trans Med Imaging* 18(3):282–290
42. Boukerroui D, Baskurt A, Noble JA, Basset O (2003) Segmentation of ultrasound images: multi-resolution 2D and 3D algorithm based on global and local statistics. *Pattern Recogn Lett* 24:779–790
43. Cremers D (2006) Dynamical statistical shape priors for level set based tracking. *IEEE Trans Pattern Anal Mach Intell* 28(8):1262–1273
44. Rousson M, Paragios N (2008) Prior knowledge, level set representations & visual grouping. *Int J Comput Vis* 76(3):231–243
45. Skalska A, Turcza P, Zieli skib T, Królczyk J, Grodzicki T (2012) Left ventricle USG image segmentation using active contour model. *Procedia Comput Sci* 1:2723–2732
46. Foulonneau, Charbonnier P, Heitz F (2009) Multi-reference shape priors for active contours. *Int J Comput Vis* 81(1):68–81
47. Zhang Y, Matuszewski BJ, Histace A, Precioso F (2011) Statistical shape model of Legendre moments with active contour evolution for shape detection and segmentation. In Computer analysis of images and patterns, vol. 6854, pp. 51–58
48. Wojak J, Angelini ED, Bloch I (2010) Introducing shape constraint via Legendre moments in a variational framework for cardiac segmentation on non-contrast CT images. In VISAPP, p 209–214
49. Mohammed NB, Chinnaiya A (2011) Evolution of foetal echocardiography as a screening tool for prenatal diagnosis of congenital heart defects. *J Pak Med Assoc* 61:904–909
50. Sridevi S, Nirmala S (2016) ANFIS based decision support system for prenatal detection of Truncus Arteriosus congenital heart defect. *Appl Soft Comput* 46:577–587
51. Mumford D, Shah J (1989) Optimal approximation by piecewise smooth functions and associated variational problems. *Commun Pure Appl Math* 42:577–685
52. Pavlyukevich I (2007) Lévy flights, non-local search and simulated annealing. *J Comput Phys* 226(2):1830–1844
53. Pappula L, Ghosh D (2017) Synthesis of linear aperiodic array using Cauchy mutated cat swarm optimization. *Int J Electron Commun (AEÜ)* 72:52–64
54. Skoulli V, Tassopoulos IX, Beligiannis GN (2017) Solving the high school timetabling problem using a hybrid cat swarm optimization based algorithm. *Applied Soft Computing* 52:277–289
55. Sundararaj V (2016) An efficient threshold prediction scheme for wavelet based ECG signal noise reduction using variable step size firefly algorithm. *International Journal of Intelligent Engineering and Systems* 9(3):117–126
56. Sundararaj V, Muthukumar S, Kumar RS (2018) An optimal cluster formation based energy efficient dynamic scheduling hybrid MAC protocol for heavy traffic load in wireless sensor networks. *Comput Secur & Security* 77:277–288
57. Sundararaj V (2019) Optimal task assignment in mobile cloud computing by queue based Ant-Bee algorithm. *Wirel Pers Commun* 104(1):173–197
58. Bhaduria HS, Dewal ML (2014) Intracranial hemorrhage detection using spatial fuzzy c-mean and region-based active contour on brain CT imaging. *SIViP* 8(2):357–364

Publisher's note Springer Nature remains neutral with regard to jurisdictional claims in published maps and institutional affiliations.



M.A. Femina (Femina Maria) obtained her Bachelor's degree in Electronics and Instrumentation Engineering from Manonmaniam Sundaranar University. Then, she obtained her master's degree in Medical Electronics from Anna University. Currently, she is serving as assistant professor in Department of Electrical and Electronics Engineering at KCG College of Technology, affiliated to Anna University, Chennai. Her current research interest is in medical image processing and biomedical instrumentation.



Dr. S.P. Raajagopalan received the B.Sc. degree in Mathematics and has completed his M.Sc in Applied Mathematics from IIT Madras in 1967. He received Ph.D. degree from the Madras University. He is currently professor in the Department of Computer Science and Engineering at GKM College of Engineering and Technology, affiliated to Anna University, Chennai. He has around 40 years of teaching experience. He is the author of books namely Statistics and Operation Research, Graph Theory, and Discrete Mathematics. He has also published more than 50 papers in International Journals. His field of specialization and interests are in quantitative techniques, data processing and project management, management information system, programming languages, simulation, text generation, cryptography, and data mining. Dr. S.P. Raajagopalan is an editor for International Journal on Research and Review in Software Engineering—CSC Journals.